Annales
Geophysicae

Cluster observations and theoretical identification of broadband waves in the auroral region

M. Backrud-Ivgren[1,2], G. Stenberg[3], M. André[1,2], M. Morooka[1], Y. Hobara[4], S. Joko[4], K. Rönnmark[3], N. Cornilleau-Wehrlin[5], A. Fazakerley[6], and H. Rème[7]

[1]Swedish Institute of Space Physics, Box 537, 751 21 Uppsala, Sweden

[2]Dept. of Astronomy and Space Physics, Uppsala University, Box 515, 751 20 Uppsala, Sweden

[3]Department of Physics, Umeå University, 901 87 Umeå, Sweden

[4]Swedish Institute of Space Physics, Box 812, 981 28 Kiruna, Sweden

[5]CETP/CNRS, University of Versailles Saint Quentin, 10-12 Av. De l'Europe, 78140 Vélizy, France

[6]The Mullard Space Science Laboratory, University College London, Holmbury St. Mary Dorking, Surrey, RH5 6NT, UK

[7]Centre d'Etude Spatiale des Rayonnements, 9 avenue du Colonel Roche Toulouse, France

Abstract. Broadband waves are common on auroral field lines. We use two different methods to study the polarization of the waves at 10 to 180 Hz observed by the Cluster spacecraft at altitudes of about 4 Earth radii in the nightside auroral region. Observations of electric and magnetic wave fields, together with electron and ion data, are used as input to the methods. We find that much of the wave emissions are consistent with linear waves in homogeneous plasma. Observed waves with a large electric field perpendicular to the geomagnetic field are more common (electrostatic ion cyclotron waves), while ion acoustic waves with a large parallel electric field appear in smaller regions without suprathermal (tens of eV) plasma. The regions void of suprathermal plasma are interpreted as parallel potential drops of a few hundred volts.

Keywords. Magnetospheric physics (Auroral phenomena; Electric fields; Plasma waves and instabilities)

1 Introduction

Broadband waves in the magnetosphere are important since they can efficiently redistribute energy between particle populations. These waves may have frequencies from below one up to at least several hundred Hz, thus covering characteristic frequencies, such as the ion gyrofrequencies. Broadband waves have been observed earlier by a number of satellites and rockets in the auroral region (e.g. Gurnett et al., 1977; Wahlund et al., 1998; Kintner et al., 2000) and are sometimes called BroadBand Extremely Low Frequency (BB-

ELF) waves (e.g. Knudsen et al., 1998). The waves have been shown to be important for large-scale phenomena, such as ionospheric ion outflow (e.g. André and Yau, 1997). However, there is no consensus either concerning the identification of the wave mode(s) involved, or concerning the wave generation mechanism(s).

Previous studies of broadband emissions by sounding rockets and the Freja satellite at altitudes up to 1700 km suggest that the broadband emissions are sometimes Electrostatic Ion Cyclotron (EIC), Ion Acoustic (IA), slow ion acoustic waves (Bonnell et al., 1996; Kintner et al., 1996; Wahlund et al., 1998) or Doppler-shifted low frequency dispersive Alfvén waves (Stasiewicz et al., 2000; Lund et al., 2001; Stasiewicz and Khotyaintsev, 2001). A recent study by Backrud et al. (2004) uses new methods and extends earlier investigations to higher altitudes. Using assumed particle distributions, this study indicates that broadband emissions observed by the four Cluster spacecraft at altitudes of 4–5 Earth radii (R_E) are often well described as electrostatic linear waves in a homogeneous plasma, and are a mixture of wave modes labeled with different names.

In the present study of Cluster observations we consider the observed polarization of the broadband waves, together with a realistic plasma model based on particle observations, instead of earlier assumed particle distributions (Backrud et al., 2004). Two wave analysis methods, involving different approximations and assumptions, give consistent results concerning the wave mode identification. We find that much of the broadband emissions can be identified as a mixture of ion acoustic, electrostatic ion cyclotron and ion Bernstein waves, all of which in linear theory of waves in a homogeneous plasma can be described as different parts of the same dispersion surface (André, 1985). Ion acoustic and oblique

ion acoustic waves have also been identified by using interferometry (Backrud et al., 2005).

A new result is that ion acoustic waves occur only in relatively small regions without suprathermal (tens of eV) electrons. This observation is consistent with textbook plasma physics, stating that even low density cold Maxwellian electron distributions can damp ion acoustic waves (e.g. Brambilla, 1998). This explains both why ion acoustic waves can occur in the auroral region at all, and why they are relatively rare.

The regions void of suprathermal electrons are interpreted as structures with potential differences of a few hundred volts along the geomagnetic field, accelerating electrons downwards and stopping cold ionospheric electrons from reaching Cluster altitudes. Similar regions are often labeled "inverted-V" structures at lower altitudes. Janhunen et al. (2004) concluded from Polar data that quasi-static potential structures do not extend up to altitudes of $5\,R_E$. However, in the region of upgoing electrons (the return current region) Marklund et al. (2004) used Cluster data to confirm quasi-static potential structures at these altitudes. In their case particle data indicated that the observations were made above the acceleration region. In the context of our study, the structures causing the downward electron acceleration are important since they give rise to conditions favourable for IA waves.

Generation mechanisms suggested for broadband waves include particles streaming along the geomagnetic field. One possibility is the so-called ion-ion instability, where ion populations drift relative to each other in a field-aligned potential drop and create instabilities (Bergmann et al., 1988; Gray et al., 1990). Another possibility is electrons drifting relative to the ions (often described as a current when low energy electrons cannot be observed directly by particle detectors). Kindel and Kennel (1971) suggested that current instabilities excite parallel IA and oblique EIC wave modes. They showed that the angle of propagation for the unstable waves depends on the ratio of the electron and ion temperatures, T_e/T_i. Ganguli et al. (2002) showed that a transverse gradient in the plasma flow velocity can increase the parallel phase speed of an ion acoustic wave and sufficiently reduce ion Landau damping. This will reduce the threshold current for the current driven ion acoustic instability. Wahlund et al. (2003, and references therein) suggested that field-aligned currents associated with low-frequency Alfvén waves has can trigger ion acoustic waves. Using a realistic plasma model, including several particle distributions, we find that in the cases we have studied, field-aligned electron beams with energies of about hundred eV can generate the observed waves.

2 Instrumentation

Cluster is a four-satellite mission for detailed studies of the terrestrial magnetosphere (Escoubet et al., 1997). The orbits are approximately polar with a pergiee of $4\,R_E$ and an apogee of $19.6\,R_E$. The satellites spin at 15 rpm in a plane essentially coinciding with the GSE x-y plane. In this study

we consider in detail data from the EFW double-probe electric field and wave instrument with two pairs of probes in the spin plane of each satellite (Gustafsson et al., 1997), together with observations from the FGM fluxgate (Balogh et al., 1997) and the STAFF search coil (Cornilleau-Wehrlin et al., 1997) tri-axial magnetometers, the CIS ion (Rème et al., 1997) and the PEACE electron spectrometers (Johnstone et al., 1997). The sampling rates (filters) used during the events we consider here are for EFW and STAFF 450 Hz (band-pass between 10 and 180 Hz), and for FGM 67 Hz. To be able to study the wave polarization of broadband waves above 10 Hz we have selected events where the spacecraft instruments are in burst-mode. Also, we have selected regions where the angle between the geomagnetic field and the spin-plane of the spacecraft is small. This enables an estimation of the electric field wave components, both perpendicular and parallel to the geomagnetic field.

3 Wave and electron observations

The event in this study is from 14 February 2003 when the Cluster fleet crossed the auroral magnetic field lines at an altitude of $4.2\,R_E$ in the Northern Hemisphere at $\sim$0.8 MLT. In this study we show data from spacecraft 1, 2 and 4 while spacecraft 3 arrives much later. The spacecraft were configured as pearls on a string with velocity vectors for all three spacecraft almost perpendicular to the ambient magnetic field, with a speed of approximately 4–5 km/s. The separation between the spacecraft was a few thousand km.

Figure 1 shows 40 min of data between 14:13:00–14:53:00 UT for Cluster spacecraft 4 (C4). Panels (a) and (b) display the perpendicular ($\delta E_\perp$) and parallel ($\delta E_{||}$) components of the electric field, and panels (c) and (d) show their power spectral densities calculated by using standard FFT. In this study we focus on waves well above the gyrofrequencies, which are 7.6 Hz (H$^+$) and 0.47 Hz (O$^+$) for this event. From particle data we estimate the abundance of protons to be one-third, and O$^+$ to be two-thirds of the total density of $5\,\mathrm{cm}^{-3}$ estimated from the observed plasma frequency. The lower hybrid frequency is then calculated to be 160 Hz. There are three larger regions with broadband emissions (14:14–14:19 UT, 14:25–14:36 UT and 14:43–14:51 UT), where $\delta E_\perp$ is larger than $\delta E_{||}$ most of the time. There are two short time intervals where $\delta E_{||}$ is in fact larger than $\delta E_\perp$ (around 14:31:00 UT and 14:44:00–14:46:10 UT), with N peak-to-peak amplitude up to 100 mV/m. The waves appear in bursts and last for a fraction of a second up to one second, in this event, which is typical for waves with $\delta E_{||}/\delta E_\perp \geq 1$ on auroral magnetic field lines at these altitudes (see also Backrud et al., 2004).

Panel (e) in Fig. 1 shows upgoing electrons while panel (f) shows downgoing electrons. The black region between 14:30:00–14:30:40 UT is a data gap. It is possible to distinguish a typical structure in both upgoing and downgoing electron energy spectra from the PEACE instrument during the two time sequences when $\delta E_{||}/\delta E_\perp \geq 1$ (around
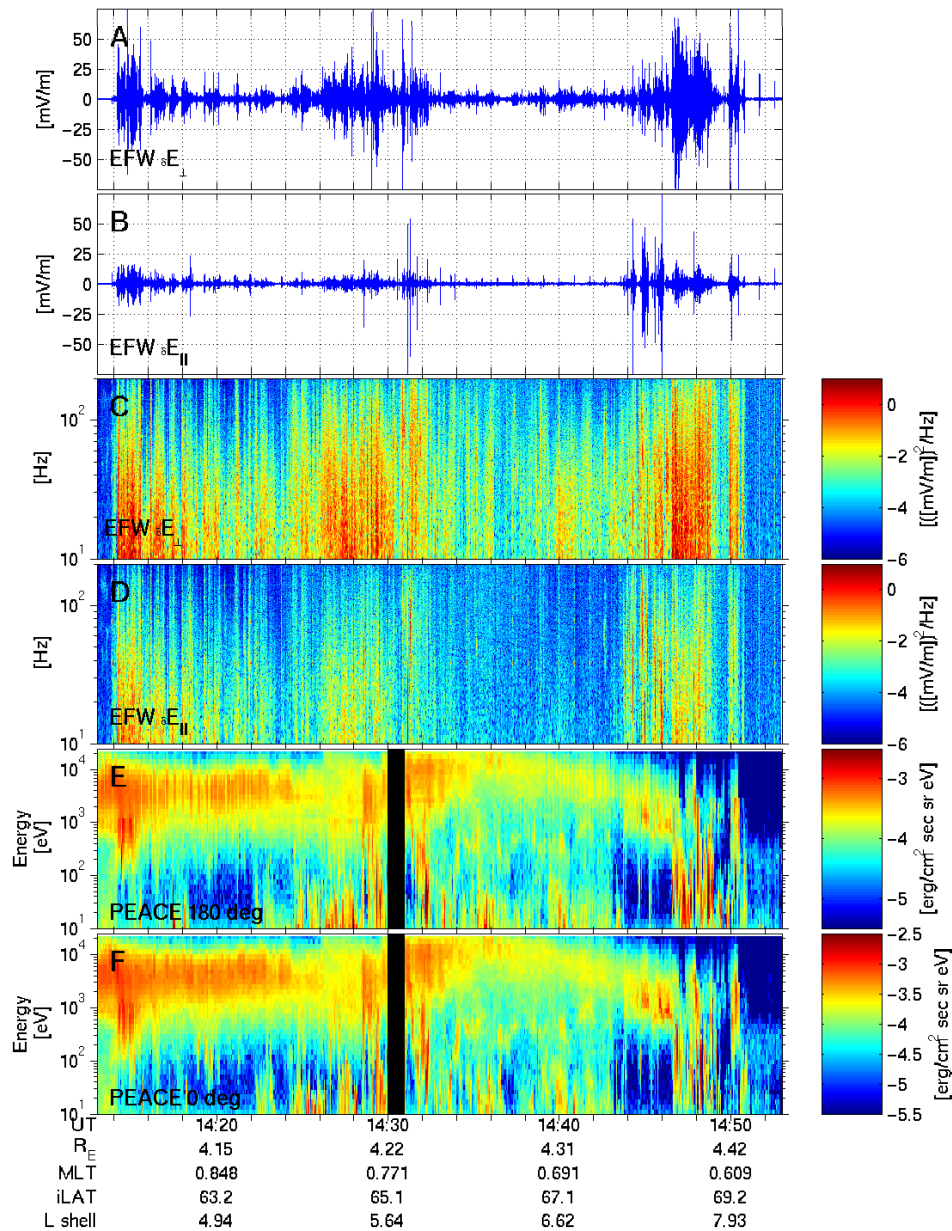
Fig. 1. Data observed by Cluster spacecraft 4 during a crossing of an auroral magnetic field line: electric field (10–180 Hz) perpendicular (panel **A**) and parallel (**B**) to the ambient magnetic field; spectra of perpendicular (**C**) and parallel (**D**) electric field; energy spectra of downgoing (**E**) and upgoing (**F**) electrons. Waves with a large parallel component of the electric field are found in regions without cold electrons. The H^+ gyrofrequency and the lower hybrid frequency are 7.6 Hz and 160 Hz, respectively.

14:31:00 UT and 14:44:00–14:46:10 UT). There are essentially no suprathermal (tens of eV) electrons observed and the high-energy (keV) electron flux is increased. These observations are consistent with the hypotheses that the spacecraft is flying through a potential structure where the electrons above the spacecraft are accelerated downward and the suprathermal ionospheric electrons below the spacecraft could not penetrate the barrier at the bottom of the potential structure.

Electron observations consistent with quasi-static potential structures have, to our knowledge, not been reported from altitudes around 4–5 R_E. Such structures observed at lower altitudes are often called "inverted Vs" because of their appearance in energy-time electron spectrograms. Potential minima have been observed by the Polar spacecraft (Janhunen et al., 2004) at altitudes of 4–6 R_E. However, the authors' interpretation of these observations was that the potential minima probably were temporally evolving structures created by low frequency Alfvén waves. As will become clear later, for our detailed wave study, the lack of suprathermal electrons is interesting, while the exact cause of the observed particle distributions is not essential.
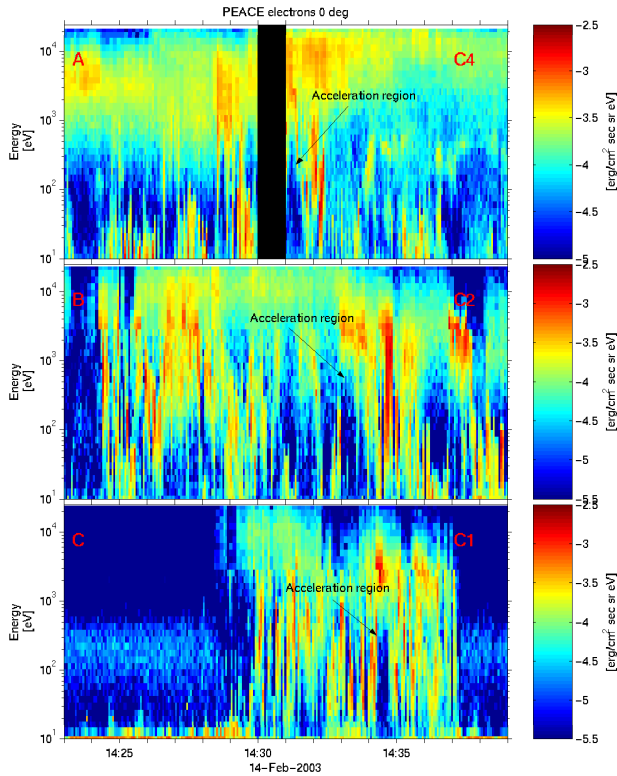
Fig. 2. Energy spectra of downgoing electrons from Cluster spacecraft 4 (panel (**A**)), 2 (**B**) and 1 (**C**). An acceleration region observed by all spacecraft is indicated.

To estimate $\delta E_{||}$ in Fig. 1, we have assumed that the angle θ between the ambient magnetic field and the spin-plane of the spacecraft is small, i.e. $\theta < 23°$, during the 40 min of data. In the two regions where emissions with large $\delta E_{||}$ are detected (around 14:31:00 UT and 14:44:00–14:46:10 UT), $\theta < 8°$. For this type of study (see also Backrud et al., 2004), we assume that the second perpendicular component (perpendicular to both the ambient magnetic field and the observed perpendicular electric field) of the electric field is zero. The observed wave field can then be divided into one perpendicular and one parallel component of the electric field. To test the credibility of this assumption we have tested the opposite scenario, i.e. that the observed, nearly parallel electric field is due to a large wave field perpendicular both to the ambient magnetic field and to the observed perpendicular wave component. This scenario essentially always gives such an assumed perpendicular field at least ten times larger than the observed perpendicular wave component. Thus, for $\delta E_{||}/\delta E_{\perp} \geq 1$, the error of the estimated parallel electric field is likely to be less than 10%.

The region with $\delta E_{||}/\delta E_{\perp} \geq 1$ and the corresponding acceleration region between 14:44:00–14:46:10 UT is only seen by C4, while the emissions with larger $\delta E_{||}$ than $\delta E_{\perp}$ around 14:31:00 UT is also detected on Cluster spacecraft 2 (C2) and spacecraft 1 (C1). The spacecraft are configured as pearls on a string, with C4 leading C2 by 4000 km mainly in the z_{gse}

direction and C2 leading C1 by 3000 km, also mainly in the z_{gse} direction. The satellite velocity vectors are nearly perpendicular to the geomagnetic field with a speed of 4–5 km/s. Cluster spacecraft 3 is not shown in this study because it is far behind (15 000 km behind C1, corresponding to ∼7 min calculated with the plasma drift velocity, see below).

Figure 2 shows downgoing electrons from the three leading spacecraft. One of the observed acceleration regions mentioned in Fig. 1 is now in highlighted Fig. 2 with an arrow (panel a). The region starts at 14:31:00 UT, (right after a data-gap, black region) and lasts for 35–40 s. Panel (b) shows a similar region between 14:33:00–14:33:35, where essentially no suprathermal (tens of eV) electrons are observed while the high-energy electron flux is increased. We also interpret this to be an acceleration region (seen by C2) but it is not as obvious as in C4. However, by looking carefully through the time sequence, this region (pointed out with an arrow) is the only sequence without cold electrons and with an increase in the flux of higher energy electrons. The time difference between the observations of the acceleration regions by C4 and C2 is 120 s. This implies a plasma drift of approximately 35 km/s in the z_{gse} direction, assuming that the acceleration region is spatial and flowing over the spacecraft. Also on C1 it is possible to see a similar region (panel c, pointed out with an arrow) at 14:34:20–14:34:55 UT, which we again interpret to be an acceleration region. It is observed 80 s after it was detected by C2, which implies that the same speed and direction of the plasma drift is needed between C2 and C1 to observe the same region. The needed plasma drift is consistent with the $E \times B$ drift estimated from the EFW and FGM instruments of approximately 30–40 km/s.

Our interpretation of the electron observations is that the acceleration region, observed at this passage at an altitude of ∼4 R_E, is spatial, flowing over the spacecraft with the plasma drift and is stable over at least a couple of minutes. Similar to C4, there are also broadband emissions with $\delta E_{||}/\delta E_{\perp} \geq 1$ inside the acceleration region in C2 and C1. However, it is not possible to identify the same emission on two spacecraft, which implies that the waves are much more short-lived than the acceleration region itself.

Backrud et al. (2004) concluded that the $\delta E/\delta B$ ratio of electrostatic broadband waves between 10–180 Hz on auroral magnetic field lines varied in a structured way with respect to the $\delta E_{||}/\delta E_{\perp}$ ratio. Their interpretation was that broadband waves are a mixture of emissions consistent with various wave modes.

Figure 3 shows how the $\delta E/\delta B$ ratio varies with $\delta E_{||}/\delta E_{\perp}$ for the 40 min of data displayed in Fig. 1. The data points form a "V" which is consistent with the above-mentioned analysis by Backrud et al. (2004). Since the waves are interpreted as electrostatic waves, the $\delta E/\delta B$ ratio is varying in a systematic way as a function of the direction of the k-vector. The data points correspond to sub-intervals of the data with a frequency resolution of ∼15 Hz and a time resolution of 0.1 s, using a standard FFT. Green (10–40 Hz) and red (40–100 Hz) dots are present but not visible beneath the
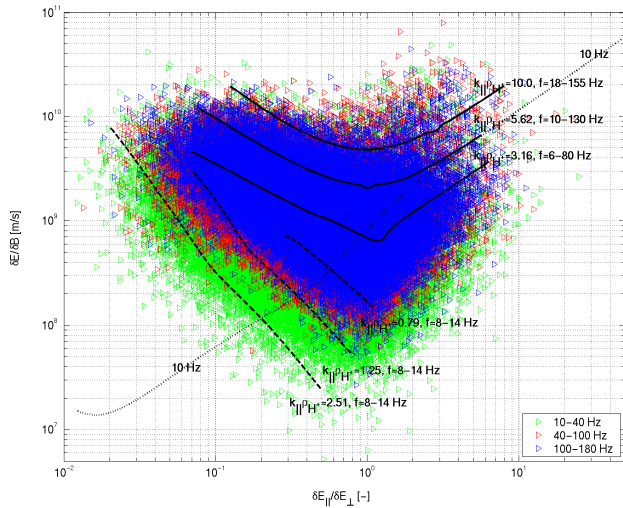
Fig. 3. The 40-min time period in Fig. 1 is divided into sub-intervals of 0.1 s using a standard FFT. Different colours correspond to different frequency intervals. Green and red dots are present but not visible beneath the blue dots. The lines are theoretically estimated as $\delta E/\delta B$ ratios for different frequencies and different k-vectors. See text for details.

Fig. 4. A detail of the event in Fig. 1. Perpendicular (panel **A**) and parallel (**B**) components of the electric field; upgoing (**C**) and downgoing (**D**) electron energy spectra. There is a sharp boundary (around 14:46:40 UT) with a dramatic change in both the electric field (A and B) and in the electron data (C and D). Waves with a large parallel component of the electric field are only observed when there are no cold electrons detected. There is an overall good correlation between wave emissions and electron distributions.

blue (100–180 Hz) dots. Data points below the noise level of the instruments are removed (Backrud et al., 2004). Here we choose to call waves with the $\delta E_{||}/\delta E_{\perp}$ ratio of around one or larger ion acoustic or oblique ion acoustic, while a $\delta E_{||}/\delta E_{\perp}$ ratio of around one or smaller here corresponds to electrostatic ion cyclotron waves or ion Bernstein waves. A $\delta E_{||}/\delta E_{\perp}$ ratio of around one or larger is consistent with ion acoustic or oblique ion acoustic waves, while a $\delta E_{||}/\delta E_{\perp}$ ratio of around one or smaller is consistent with electrostatic ion cyclotron waves and perhaps ion Bernstein waves. There is no sharp boundary between the waves modes labeled with different names. Thus, during the 40-min interval, we find a mixture of emissions consistent with various wave modes. The lines in the figure and the wave modes will be discussed in detail later in the theory section.

Broadband waves between 10–180 Hz, with $\delta E_{||}/\delta E_{\perp} \geq 1$, have in this study only been detected in regions without suprathermal electrons. Figure 4 shows details of the event in Fig. 1. We can again see the characteristics of an acceleration region in the electron distributions (panels c and d) between 14:43:50–14:46:35 UT. The corresponding broadband waves with a large $\delta E_{||}$ component are displayed in panel (b). At a few times during this time interval, cold electrons (up to a few tens of eV) are detected (~14:44:40 UT, ~14:45:20 UT, ~14:45:45 UT) and the emissions with a large $\delta E_{||}$ component are at these times damped. Also, the wave-characteristics change dramatically after 14:46:35 UT, where the $\delta E_{\perp}$ component (panel a) is instead much larger than the $\delta E_{||}$ component (panel b). At the same time, there is also a sharp boundary detected in both the up- and downgoing electrons, clearly showing the presence of suprathermal electrons at later times. Thus, even at the highest resolution
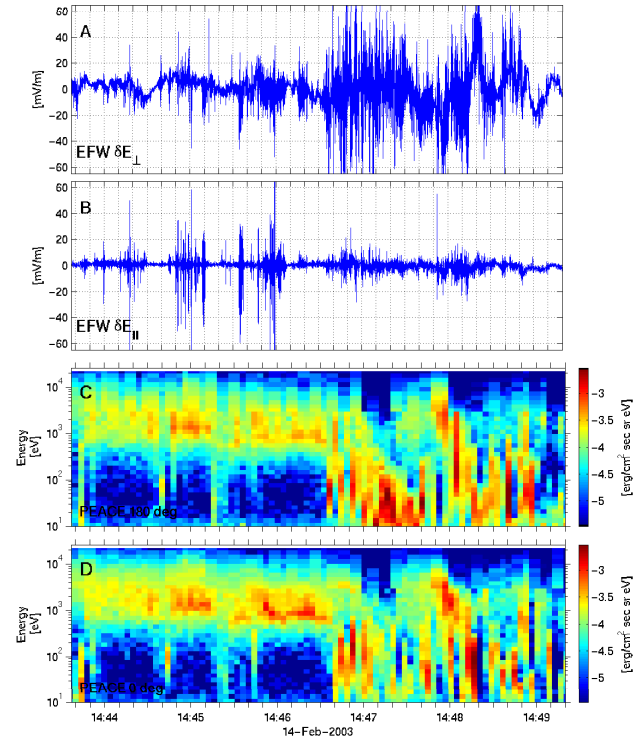
possible to routinely obtain full electron distributions (the spacecraft spin of 4 s), there is a clear correlation between large fluctuating parallel electric fields and the absence of suprathermal electrons.

Figure 5 shows another detail of Fig. 1. This is yet another example of a good correlation on smaller scales between waves with a large $\delta E_{||}$ component (panel b) and the absence of suprathermal electrons (panels c and d). The waves with a large $\delta E_{||}$ component are excited around 14:31:10 and between 14:31:17–14:31:19 UT, i.e. only when the suprathermal electron population is missing. The highlighted yellow wave sequence will be studied further in detail in the theory section.

From Figs. 1–5 we can conclude that waves with a $\delta E_{||}/\delta E_{\perp}$ ratio ≥ 1 exist in short bursts of a fraction of a second, up to one second. These bursts occur in regions where essentially no suprathermal electrons are detected.

4 Modeling the plasma

Figure 3 and the results in Backrud et al. (2004) suggest that the observed waves can be described within the framework of linear waves in a homogeneous plasma. In order to examine
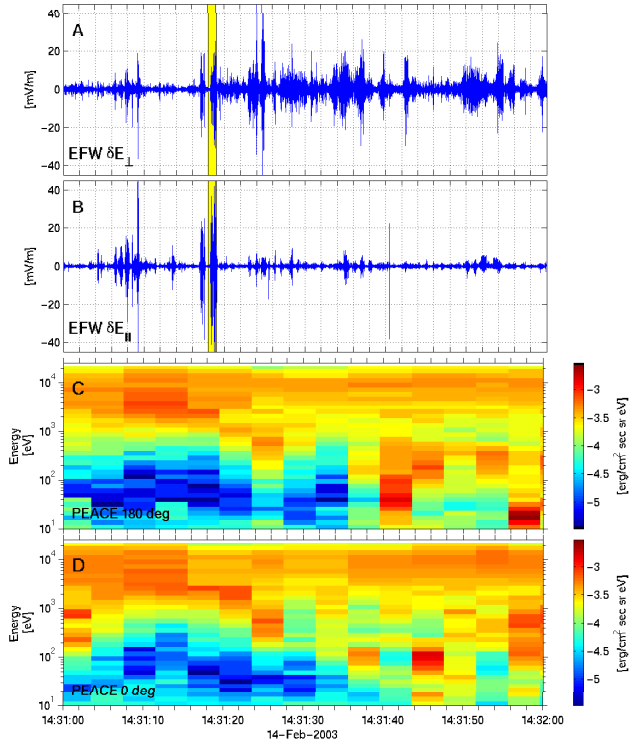
Fig. 5. A detail of the event in Fig. 1. Another example of waves with larger parallel (panel **B**) than perpendicular **(A)** component of the electric field which shows good correlation with electron distributions without cold electrons (**C** and **D**). The yellow sequence (panels A and B) will be studied further in detail in Fig. 6 and in the theory section in Figs. 10–12.
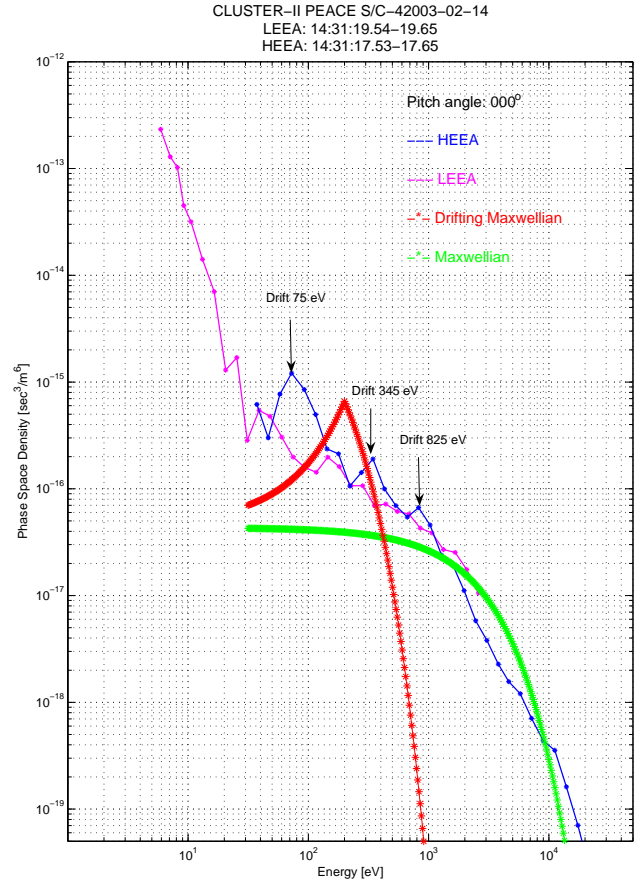

Fig. 6. PEACE instrument data showing phase space density for downgoing electrons from the sensors HEEA (blue line) and LEEA (magenta line). One ordinary Maxwellian distribution (green line) and one drifting Maxwellian distribution (red line) with energy of 200 eV will represent typical electron populations in the theory section.

to what extent such a theoretical description is consistent with the observations we model the plasma. The model is produced with two purposes. Firstly, we seek to explain the V-shape in Fig. 3 in terms of the linear wave modes present in a realistic plasma environment. Secondly, we intend to analyze in detail a short (1 s) burst of waves with large $E_{||}$ (highlighted in Fig. 5). To meet both of these requirements we base the plasma model on particle observations made at the time of the selected short burst (14:31:18–14:31:19 UT), and argue that the plasma parameters do not vary much since the V-shape is preserved over a long time period. We use data from Cluster 4, as all particle and wave instruments work properly on this spacecraft.

At the time of interest the background magnetic field is 600 nT. Interpreting the strong signal at 20 kHz detected by the resonance sounder WHISPER (Décréau et al., 1997) as the plasma frequency, the density is estimated to 5 cm^{-3}. In the following paragraphs we model the particle distributions.

5   Electrons

The PEACE instrument has two sensors, LEEA and HEEA. They are mounted on opposite sides of the spacecraft, such

that they have the same field of view every two seconds (one-half of a spacecraft spin).

Figure 6 shows the phase space density for the electrons. LEEA (magenta line) is observing the downgoing electrons around half a second after the event we study in the theory section. HEEA has the same field of view two seconds earlier than LEEA and therefore observes downgoing electrons less than half a second before the wave emissions. The two sensors observe different electron distributions, indicating rapid variations in time or space. The HEEA observations before the wave event show multiple beams (75 eV, 345 eV and 825 eV) which might generate waves. There are two Maxwellian functions in the figure representing the typical background and beam electron distributions in the wave generation region. The green line is a Maxwellian distribution with a density of 4.5 cm^{-3}, and the red line is a drifting Maxwellian distribution with a drift energy of 200 eV, with a density of 0.5 cm^{-3}.

At the lowest detector with energy levels of a few eV the electron observations may be contaminated by
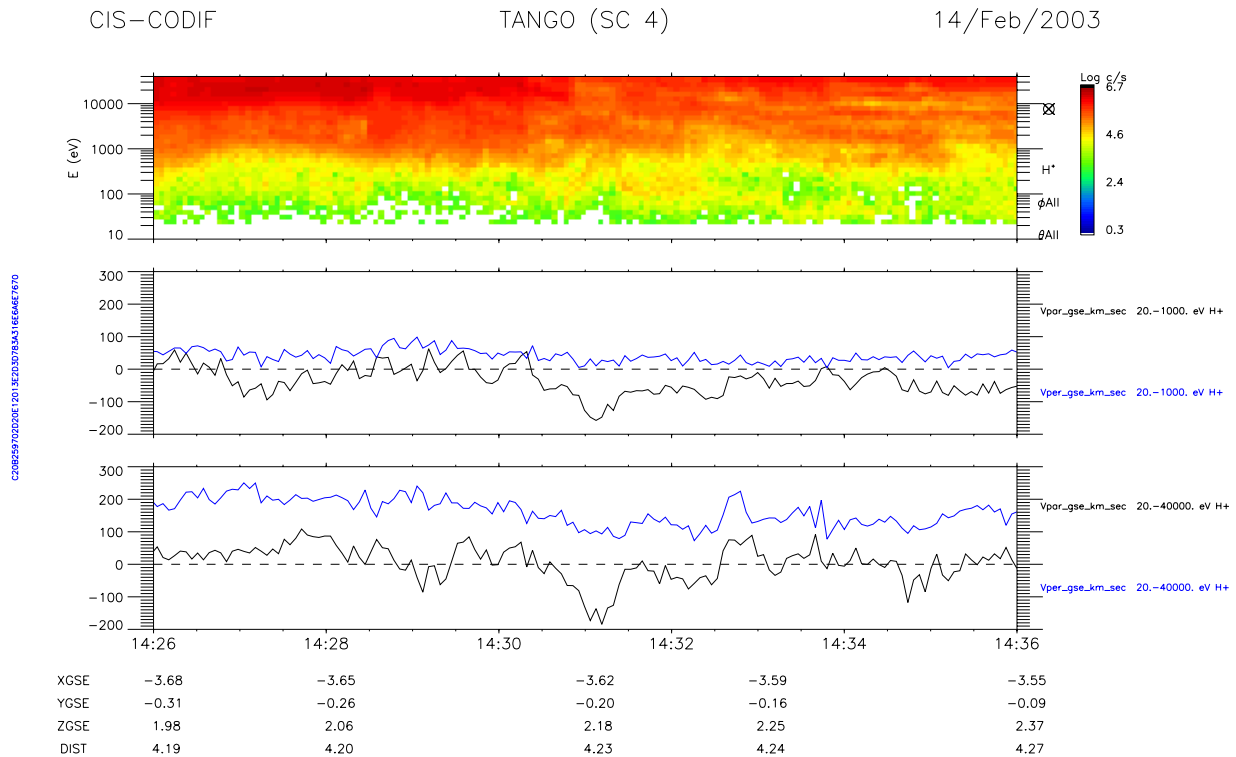
Fig. 7. Energy-time spectrogram of H^+ observed by the CIS instrument (panel (**A**)). We distinguish a cold (100 eV) and a hot (4.5 keV) component. Panels (**B**) and (**C**) show estimated parallel and perpendicular velocities for the cold H^+ and the hot H^+ component, respectively.

photoelectrons from the spacecraft. The EFW instrument shows that the probe-to-spacecraft potential is about 5 V and observations below 10 eV are removed in Fig. 6. During the short time interval of Fig. 6, there are also clear indications of electrons at energies between 10 and 30 eV. As is clear from the electron spectrograms in Fig. 5, the electron flux at these energies is strongly varying. The particle observations and the overall variable situation suggest that during a significant part of the event a simple model without any suprathermal electron population can be used. As will become clear, the absence or at least the low density of suprathermal electrons is of interest for the growth of IA waves.

5.1 Ions

The CIS ion spectrometer reveals a region with a mixture of cold upgoing ionospheric H^+ and O^+ and hot magneto-spheric (H^+ and O^+) ions. To ensure quasi-neutrality the total ion density is taken to be 5 cm^{-3}. At the time of the selected waves there is a predominance of O^+ ions and the density ratio between O^+ and H^+ is approximated to 2.

Figure 7 shows the protons as observed by the CIS instrument. The top panel presents the particle flux versus time and energy. We chose to model H^+ as two different plasma components, with energies of 100 eV and 4.5 keV, respectively. The cold component is difficult to distinguish in Fig. 7, especially at the beginning of the time interval shown. Both components are modeled as (drifting) Maxwellians, and the

density ratio between the hot and the cold component is 3/2. Reasonable parallel drift velocities can be read from the second and third panels. The second panel shows parallel and perpendicular bulk velocities for the cold component, that is, velocities are calculated integrating over energies in the range 0–1000 eV. The third panel presents corresponding parameters for the hot component. Seconds prior to our event at 14:31:18–14:31:19 UT there are dips in the parallel velocities (i.e. larger parallel drifts anti-parallel to the ambient magnetic field). We regard these large drifts neither as necessary for the intense wave burst nor as representative of the whole time period and therefore use more moderate drifts. Hence, the parallel drift of the cold component is approximated to -70 km/s. The minus sign indicates that the ions drift anti-parallel to the background magnetic field, that is, upward from the ionosphere. The drift velocity of the hot component is set to zero, as the observed drift is just a small fraction of the thermal velocity and is not likely to affect the wave mode structure.

Figure 8 presents corresponding data for O^+. In this case the top panel (O^+ flux versus time and energy) clearly suggests two components. Hence, the oxygen ions are also modeled using two drifting Maxwellians. The low energy population is assumed to have an energy of 200 eV and a parallel drift of -50 km/s, whereas the high energy population has an energy of 5 keV and a drift of 170 km/s. The drift velocities can be found in the two lower panels. The density ratio between the hot and cold components is 1.
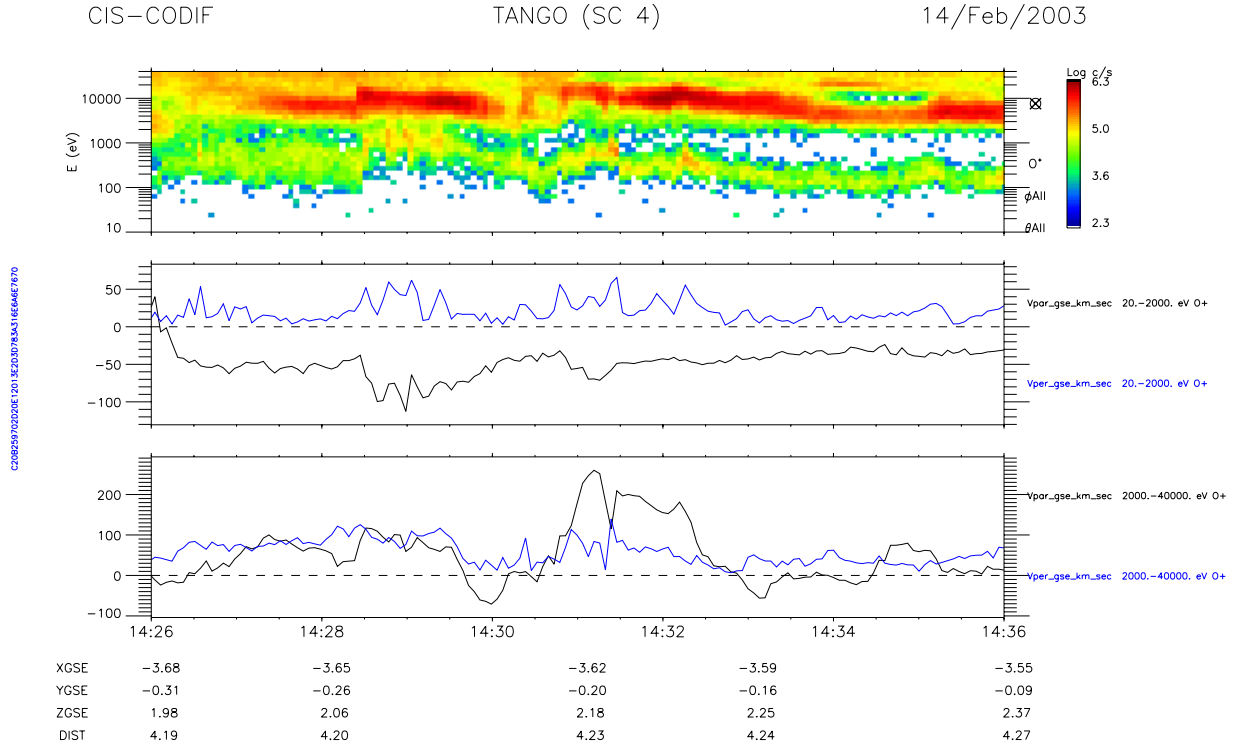
Fig. 8. Energy-time spectrogram of O^+ observed by the CIS instrument (panel **(A)**). We distinguish a cold (200 eV) and a hot (5 keV) component. Panels **(B)** and **(C)** show estimated parallel and perpendicular velocities for the cold O^+ and the hot O^+ component, respectively.

Table 1. Plasma model.

	n (cm^{-3})	$T_\parallel = T_\perp$ (eV)	$v_\parallel$ (km/s)	$v_\parallel / v_{th}$	
H^+	0.67	100	−70	−0.5	
H^+	1	4500	0	0	
O^+	1.66	200	−50	−1.0	B_0=600 nT
O^+	1.67	5000	170	0.7	$v_{E \times B}$=30 km/s
e^-	0.5	75	8700	1.7	
e^-	4.5	2000	0	0	

The CIS instrument also provides an estimate of the plasma drift velocity. The perpendicular component in the two lower panels of Figs. 7 and 8 can be interpreted as the drift velocity. Except for the hot H^+-component, they all yield 20–50 km/s, in good agreement with the $E \times B$ estimate of 30–40 km/s. Hence, for our modeling purposes we use a plasma drift velocity ($v_{E \times B}$) of 30 km/s in the z_{gse}-direction. The resulting plasma model is summarized in Table 1.

The $v_{E \times B}$ in the z_{gse}-direction is included in the WDF analysis, but cannot be included in the model used in the basic version of the dispersion solver WHAMP.

6 Linear wave modes

In order to investigate the mode structure of linear waves in the plasma described by Table 1, we use the dispersion solver

WHAMP (Rönnmark, 1982). In the frequency range of interest, above the proton gyrofrequency but below the lower-hybrid and plasma frequencies, we find ion-acoustic waves, together with a whistler mode and ion Bernstein waves. The complex plasma model, including several drifting components, suggests that additional ion-acoustic modes and/or beam modes might be possible. However, for this model we cannot find any such modes. The following analysis focusses on the ion-acoustic mode, which is the only available mode with a considerable growth rate and also the only mode with $\delta E/\delta B$ and $\delta E_\parallel/\delta E_\perp$ in accordance with observations. In Fig. 9a the solution to the dispersion relation is presented as constant frequency contours versus normalized wave vector components, parallel ($k_\parallel \rho_{H^+}$) and perpendicular ($k_\perp \rho_{H^+}$) to the background magnetic field. Here ρ_{H^+}=16 km is the gyroradius of the hot protons in the plasma model. The usual
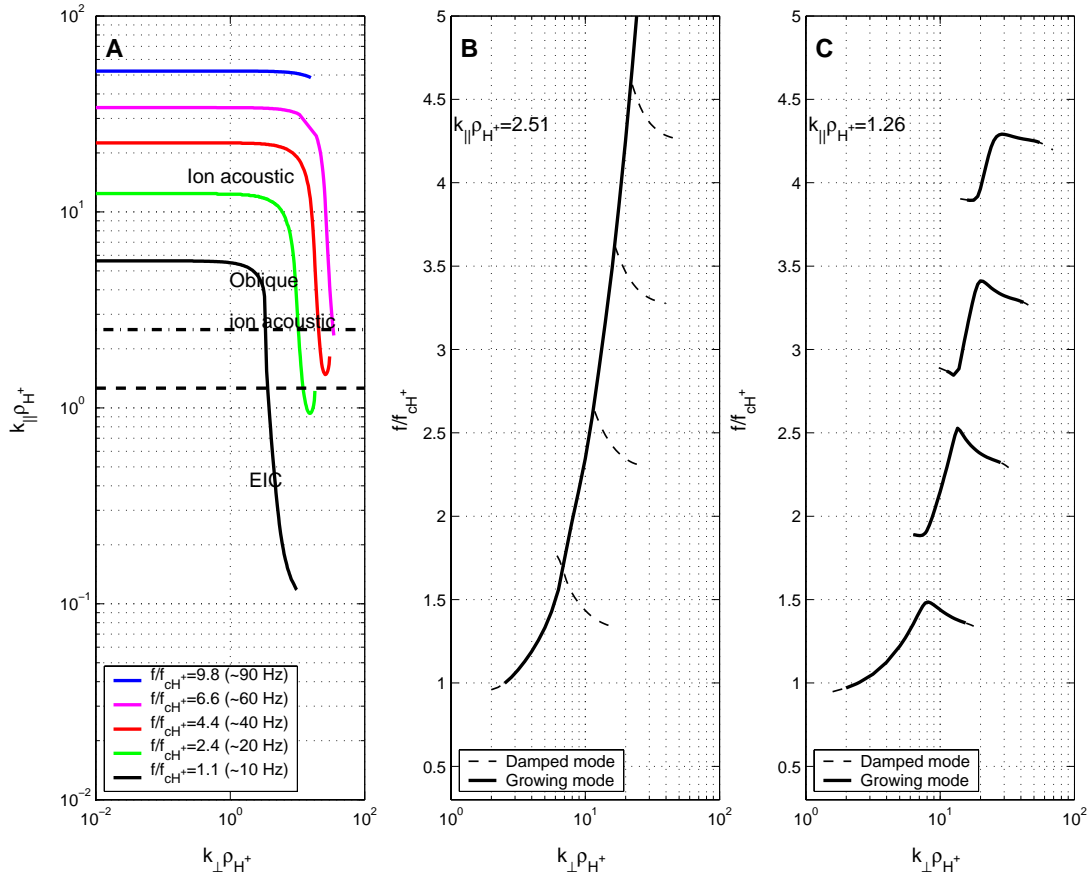
Fig. 9. The solution to the dispersion relation **(A)**. Contours of constant frequency are plotted versus normalized parallel and perpendicular wave vectors. Here ρ_{H+}=16 km is the gyro radius of the 4.5 keV protons in the plasma model. We identify the wave located on different parts of the dispersion surface as ion acoustic, oblique ion acoustic and Electron Ion Cyclotron (EIC) waves. The two horizontal lines indicate the location of the cross sections in panels (B) and (C). The oblique ion acoustic mode is continuous in frequency as is seen by a cross section at $k_{\parallel}\rho_{H+}$=2.51 **(B)**. At smaller parallel wave vectors the dispersion surface is fragmented and consists of ridges associated with the H$^+$ harmonics **(C)**.

ion acoustic mode is identified as waves with $k_{\parallel}/k_{\perp}>1$. At $k_{\parallel}/k_{\perp}\approx 1$, the solution is difficult to find and the dispersion surface makes a fairly sharp turn in wave vector space.

Figures 9b and c show cross sections at fixed parallel wave vectors, presenting frequency versus $k_{\perp}\rho_{H+}$. There is a clear change in the mode structure as we move in the $k_{\parallel}$-direction. For relatively small parallel wave vectors (Fig. 9c) we observe a banded structure. Growing waves reside on ridges associated with the proton cyclotron harmonics. We refer to this fragmented mode at smaller $k_{\parallel}\rho_{H+}$ as Electrostatic Ion Cyclotron (EIC) waves. For larger parallel wave vectors (Fig. 9b) the dispersion surface is continuous, passing through all multiples of the proton gyrofrequency. However, while this continuous mode is growing there is a damped remnant of the banded structure at larger perpendicular wave vectors. These bands connect to the continuous mode. We refer to the waves located on the continuous mode as oblique ion acoustic waves.

With several plasma populations drifting with respect to each other, there is a surplus of free energy available for

wave growth. In this case the drifting electrons seem to be the primary cause of wave growth. If we set all ion drifts to zero, the ion acoustic mode is still growing. For parallel propagation we find that below an electron drift velocity of v_d/v_{th}=1.2 there is no growth above the proton gyrofrequency. The growth rate increases with increasing drift velocity up to v_d/v_{th}=1.5. For drifts larger than v_d/v_{th}=2.0 the ion acoustic mode is again damped. The behavior is similar for more oblique propagation.

As previously discussed in this paper, waves with large $\delta E_{\parallel}$ coincide with regions void of suprathermal electrons. Hence, there are no suprathermal (non-drifting) electrons included in the model we use. Adding such a component changes the instability drastically. Introducing less than a 1% amount of 20 eV electrons quenches the instability at the ion acoustic and oblique ion acoustic modes. Note that growing ion acoustic waves requires both the absence of suprathermal electrons to avoid damping and the presence of an energy source, such as a beam, to cause growth. The EIC waves are less affected, and these waves may exist even in an
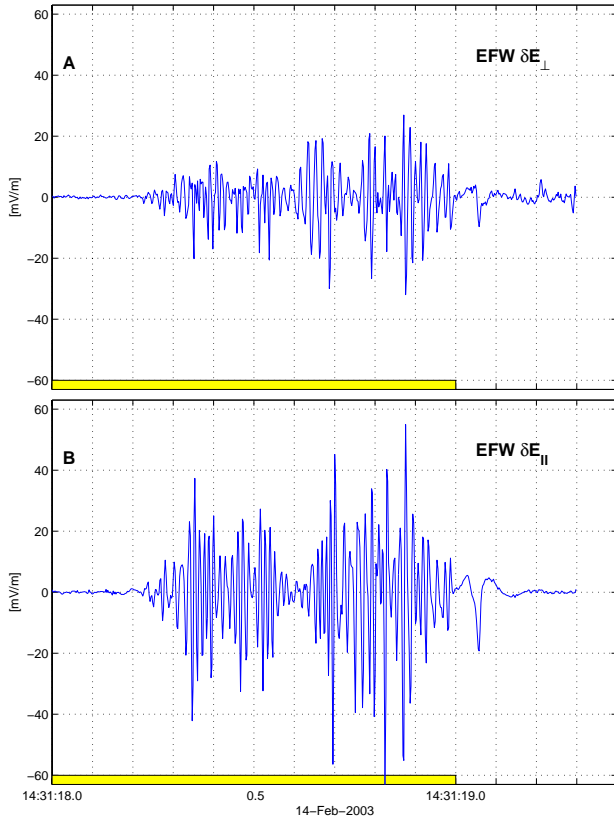
Fig. 10. For 1.3 s of data, including the one-second period highlighted in yellow (also in Fig. 5) showing perpendicular (panel **A**) and parallel (**B**) components of the electric field. By visual inspection, the waveform during the first second (yellow) indicates that linear theory may be applicable but the structure at around 14:31:19.05 might be of a more nonlinear origin. See text for details.

environment with a small amount of suprathermal electrons. In theory a suprathermal electron component can give rise to fast growing electron acoustic waves with a phase velocity slightly larger than the thermal velocity of the cold electrons and frequencies of almost up to the electron plasma frequency. However, waves in this frequency range are not observed and in a more realistic plasma including, say, a non-drifting electron component at 50–60 eV, they are damped.

The wave modes presented in Fig. 9 are not very sensitive to the relative densities of the two O^+ components and the hot protons. Changes in the temperatures of these components or their drift velocities also result in minor variations. However, the density and temperature of the cold protons are essential parameters. Changing these parameters affects the phase velocity and the growth rates. It can be noted that the phase velocity (190 km/s) of the ion acoustic waves is slightly higher than the thermal velocity of the 100 eV protons (138 km/s). The hot electron temperature also plays an important role. We conclude that the cold protons, together with the hot electrons constitute the basis for the existence of the ion acoustic waves, and that the electron beam supplies the free energy needed for growth.

We are now ready to relate the linear wave modes presented above to different parts of the V-shaped structure in Fig. 3. The solid lines correspond to the ion acoustic and oblique ion acoustic mode. They are obtained keeping $k_{||}$ fixed and increasing $k_\perp$. Hence, by comparing with Fig. 9 (panel a), we realize that the frequency must vary along the curves. Starting to the right in Fig. 3 (large $\delta E_{||}/\delta E_\perp$) and moving left, the frequency is almost constant until $\delta E_{||}/\delta E_\perp$ is approximately equal to one. At this point the solid lines make sharp turns and the frequency begins to increase. These sharp turns correspond to the equally sharp bends in the constant frequency contours of Fig. 9 (panel a). At smaller parallel wave vectors we can move across the ridges (panel c). Keeping $k_{||}$ constant and moving across the ridge associated with the first harmonic yield the dashed lines. Along these lines the frequency does not change much. In the cases shown in Fig. 3 the frequency ranges between 8–14 Hz. Finally, a constant frequency contour on 10 Hz is also drawn in Fig. 3 (dotted line). Moving from right to left along this curve the wave vector changes from being nearly parallel to the ambient field to being more perpendicular.

We state that there is a good correspondence between the observed waves and the linear wave modes found. Moving around in the mode structure can reproduce the V-shape of Fig. 3.

7   A detailed investigation

Returning to the selected burst of waves we first take a closer look at the time series. Figure 10 shows an enlarged picture of the perpendicular (panel a) and parallel (panel b) component of the electric field, displayed earlier in Fig. 5 (highlighted in yellow). The smooth wave packets suggest that linear theory may be applicable to this particular one-second period of data. However, the structure observed at ∼14:31:19.05 UT might be of a more nonlinear origin and it is not included in the detailed study.

Repeating the procedure leading to Fig. 3, but using only the selected one-second of data results in Fig. 11. The data points are divided into three frequency intervals. On top of the data we display the constant frequency contours on 10, 40, 60 and 90 Hz. We see that the theory agrees well with the observations. The theoretical curves pass through the data points and $\delta E/\delta B$ is larger at higher frequencies, both according to theory and in the measurements. However, the observed $\delta E/\delta B$ seems to be somewhat lower than the model predicts. One reason for this is that when calculating the ratio from the data we set the non-measured $\delta E_\perp g$ component to zero. Hence, only two electric field components are used and $\delta E/\delta B$ is underestimated.

In Fig. 12 we present the power spectral density in the electric wave field versus frequency. This is compared to the temporal and spatial growth rates provided by WHAMP. The spatial growth rate is defined as the temporal growth rate divided by the group velocity. Referring to Fig. 11 we see that $k_{||}/k_\perp$ is ranging from 0.5 to 5, and we believe that
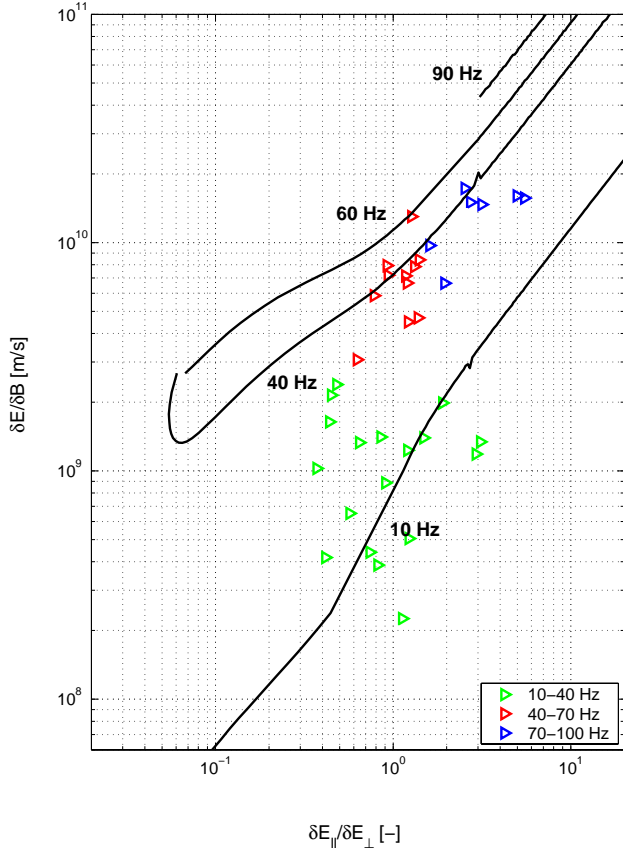
Fig. 11. A short burst of waves is analyzed using the same technique leading to Fig. 3. The data points (triangles) are divided into three frequency intervals. On top of the data points we present constant frequency curves obtained using the dispersion solver WHAMP.

Fig. 12. Comparison between the observed spectral densities (computed using the electric field), and the temporal and spatial growth rates predicted by theory. In panel **(A)** we plot the growth rates versus frequency keeping $k_\parallel$ fixed ($k_\parallel \rho_{H+}=5.01$). In panel **(B)** we let $k_\perp$ be constant ($k_\perp \rho_{H+}=1.58$).

the waves are located close to the bending of the constant frequency contours in Fig. 9. Hence, in the top panel (a) the growth rates plotted are obtained at a fixed $k_\parallel \rho_{H+}=5.01$, whereas panel (b) displays the growth rates found with a constant $k_\perp \rho_{H+}=1.58$. There is little difference between the two panels, and the wave growth is similar for all angles, from parallel to close to perpendicular k-vectors.

From Fig. 12 we see that both temporal and spatial growth rates agree very well with the frequency profile of the spectral density. Irrespective of which of the growth rates that limit the wave growth, we can conclude that our model is consistent with the observations. The growth rate profiles are shifted towards somewhat higher frequencies if the drift of the cold H^+ ions is lowered.

8 Reconstructing the WDF

Figure 11 shows that two of the polarization parameters ($\delta E/\delta B$, $\delta E_\parallel / \delta E_\perp$) agree with the measurements. However, there is more information available. Reconstructing the Wave Distribution Function (WDF) is a systematic way of invoking all polarization information in the data, that is, amplitude
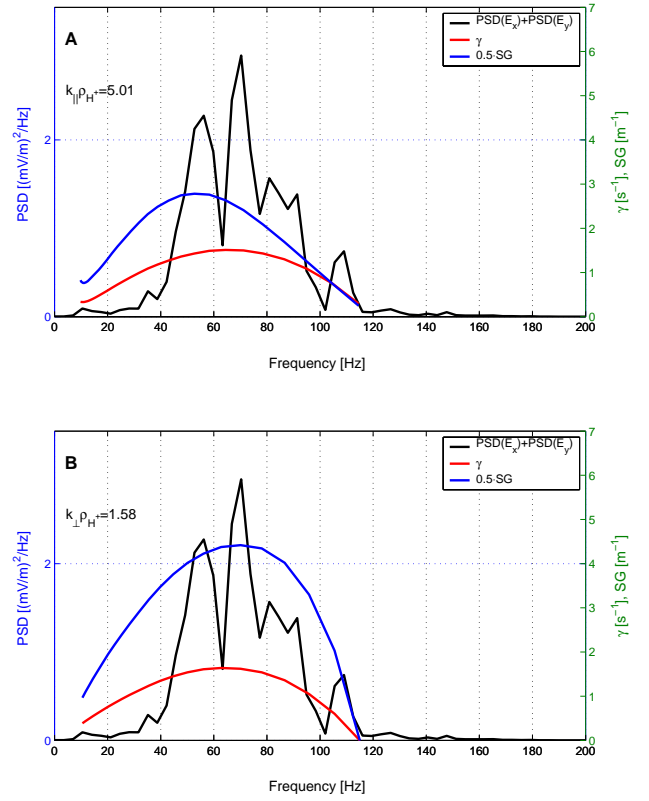
and phase relations between all wave field components. The WDF ($\psi(\mathbf{k})$) can be thought of as the wave energy density in wave vector space and is formally defined as (Oscarsson and Rönnmark, 1989)

$$\psi(\mathbf{k}) = \mathbf{E}^*(\mathbf{k}) \cdot \left[\frac{1}{\omega} \partial_\omega \mathbf{D}(\omega, \mathbf{k}) \right] \cdot \mathbf{E}(\mathbf{k}),$$

where $\mathbf{E}(\mathbf{k})$ is the Fourier-transformed electric field, $\mathbf{D}(\omega, \mathbf{k})$ is the dispersion matrix and the bracket is evaluated at $\omega = \omega(\mathbf{k})$, satisfying $\det \mathbf{D}(\omega, \mathbf{k})=0$. The WDF is related to data through the spectral matrix. For a known wave energy distribution the resulting spectral matrix can be computed. However, the inverse problem is underdetermined; an infinity of different $\psi(\mathbf{k})$ corresponds to the same spectral densities. The set of feasible solutions $\psi(\mathbf{k})$ satisfies

$$\xi[\psi(\mathbf{k})] = \frac{1}{2} \sum_{ij} \frac{|C_{ij} - S_{ij}[\psi(\mathbf{k})]|^2}{\sigma_{ij}^2} \leq \xi_{\text{bound}},$$

where S_{ij} are the theoretically calculated spectra for a given $\psi(\mathbf{k})$, C_{ij} are the observed spectra and σ_{ij} the corresponding variances. The summation is carried out over all available auto and cross spectral densities. Assuming that the errors are random and normally distributed with variances
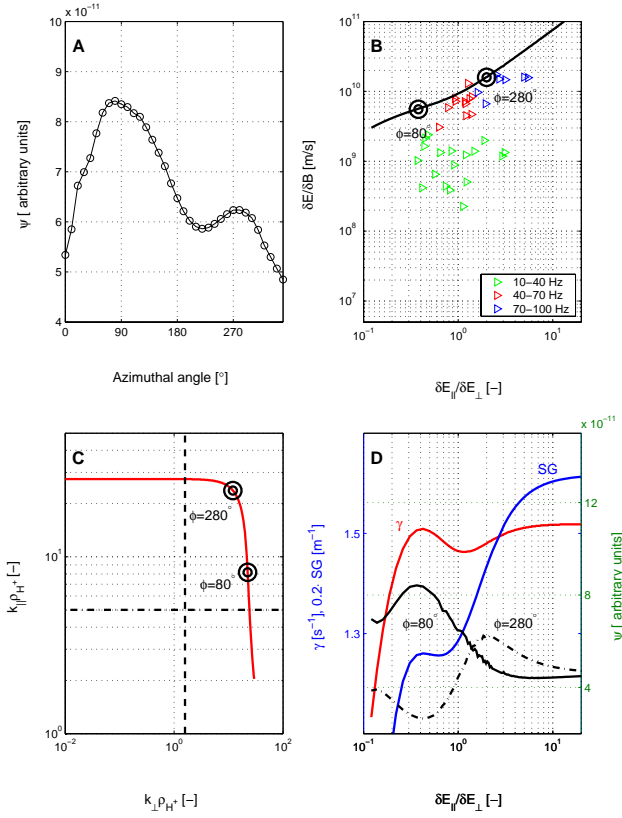
Fig. 13. Panel (**A**) presents the WDF versus the azimuthal angle. Two maxima can be identified. Panel (**B**) shows the location of these maxima on a constant frequency curve (50 Hz) plotted versus $\delta E/\delta B$ and $\delta E_{||}/\delta E_{\perp}$g. The data points are the same as in Fig. 11. The WDF maxima are also viewed on a constant frequency contour in $(k_{||}, k_{\perp})$-space (panel **C**). Panel (**D**) is a comparison between the WDF at $\phi=80°$ and $\phi=y80°$ (solid and dashed-dotted black lines) and the predicted temporal (red) and spatial (blue) growth rates.

σ_{ij}, $\xi[\psi(\mathbf{k})]$ is χ^{yg} distributed, which can be used to set an upper boundary on $\xi[\psi(\mathbf{k})]$. We chose ξ_{bound} so that, on average, the deviation of an observed spectrum from a theoretical one is one standard deviation σ. Through this approach the observational errors are included and we demand that the resulting wave energy distribution $\psi(\mathbf{k})$ produce theoretical spectral densities close to, but not necessarily identical to, the observed spectra. To select a unique solution we use a maximum-entropy algorithm. We define an entropy function as

$$H[\psi] = - \int_V d\mathbf{k}\,\psi(\mathbf{k})\ln[\frac{\psi(\mathbf{k})}{\Psi}],$$

where $\Psi=\frac{1}{V}\int_V d\mathbf{k}\psi(\mathbf{k})$. Among the feasible solutions we chose the one having the largest entropy. Our particular choice of entropy function means that when the spectra contain no information, the energy will be evenly distributed in wave vector space. Hence, we minimize the risk of introducing any artificial structure in the solutions.

The interested reader is referred to Oscarsson and Rönnmark (1989) and Oscarsson (1994) for details on the method and algorithm used. Stenberg et al. (2002) provides an example of how to apply the technique.

We reconstruct the WDF at 50 Hz, using the one-second of data presented in Fig. 10. The observational input to the reconstruction program is made up of the spectral densities at the frequency of interest. Computing the spectral densities we use a record length of 128 points and average over 6 time records. All observed wave components are used, but to avoid possible cross-correlation problems due to, for instance, phase shifts in the electronics, we do not include cross spectra between magnetic and electric wave field components. WHAMP produces the theoretical input to the reconstruction. All wave vectors satisfying the dispersion relation $\omega=\omega(\mathbf{k})$, that is, a constant frequency curve, together with the corresponding polarization vectors, are provided. It is worth pointing out that in reconstructing the WDF, we make no assumption concerning the third component of the electric field.

It is not obvious that a $\psi(\mathbf{k})$ satisfying Eq. (2) exists. However, in our case, the reconstruction scheme finds a way of distributing energy along the constant frequency curve that fulfills Eq. (2). This is in itself an important result without even considering the details of the wave energy distribution. It shows that all included polarization parameters are consistent with the wave observations. Hence, the theoretical model describes the measured waves in this sense.

The reconstructed distribution of wave energy, ψ, is expressed as a function of $k_{||}, k_{\perp}$ and ϕ. The azimuthal angle ϕ is the angle in the plane perpendicular to the ambient field. The background field is essentially in the x_{gse}-direction and $\phi=0°$ corresponds to the z_{gse}-direction. Figure 13a presents ψ as a function of ϕ. We note that there are two preferred directions, 80° and 280°. The locations of these maxima on the constant frequency curve in wave vector space are indicated by circles in Fig. 13c. Note that the angles 80° and 280° refer to the azimuthal angle. The angle between $\mathbf{k}$ and the background magnetic field is given by the ratio between $k_{||}$ and $k_{\perp}$. Since we include the Doppler shift the constant frequency curves are actually dependent on ϕ, but the variations are very small. Comparing with Fig. 9 we conclude that the waves are indeed ion acoustic or oblique ion acoustic waves. The wavelength is about 4 km. In Fig. 13b the WDF maxima (circles) are instead displayed versus $\delta E/\delta B$ and $\delta E_{||}/\delta E_{\perp}$ and compared with data. The solid line is the constant frequency contour at 50 Hz. Finally, it is interesting to compare the reconstructed WDF with the predicted growth rates. Figure 13d shows ψ versus $\delta E_{||}/\delta E_{\perp}$ at $\phi=80°$ and $\phi=280°$ (solid black and dashed-dotted black lines). In the same figure we present the temporal (red line) and spatial (blue line) growth rates. It is interesting to note that the solution seem to reflect the growth profiles even though the reconstruction tries to distribute energy as evenly as possible.

9   Discussion

Two different methods are used to compare wave and particle observations with theory, and to identify the wave modes. In both methods the observed wave polarization is compared with the polarization obtained from the theory of linear waves in a homogenous plasma. Models of the observed particle distributions are used as input to the theoretical wave dispersion relation. In the first method, two ratios of wave field components ($\delta E_{||}/\delta E_\perp$ and $\delta E/\delta B$) are compared with theory. Here we must indirectly estimate $\delta E_{||}$, and do not use all available polarization information. The advantage is that the method easily can be applied to the whole interval of several minutes, including a mixture of wave modes. In the second method, an estimate of the distribution of energy in wave vector space at 50 Hz is performed. The method is applied to a short time interval, and we focus on the detailed properties of waves with large $\delta E_{||}$. The advantage is that no assumption concerning $\delta E_{||}$ is needed and that all observed wave components are used. Both methods give fully consistent results.

The theoretical dispersion relation in Fig. 9 shows structure at multiples of the proton gyrofrequency (about 7.6 Hz) at small $k_{||}$. However, it is not likely that this structure can be observed. One reason is that with the high time resolution we use in our FFT analysis, we obtain a frequency resolution of about 15 Hz. A more fundamental reason is Doppler broadening. Oblique EIC waves have wavelengths of about 4 km. The perpendicular plasma drift of about 30 km/s dominates over the satellite velocity and gives a broadening of about 10 Hz. This would mask any harmonic structures.

Whistler mode waves and very oblique ion Bernstein waves may, in principle, be present in the frequency range that we investigate. Our polarization analysis shows that only a small part of the wave energy can be in the whistler mode. Generally, the estimated $\delta E_{||}/\delta E_\perp$ ratio is less reliable if the true $\delta E_{||}$ is small. Hence, short periods of ion Bernstein waves with electric fields close to the perpendicular direction may be missed in our statistical analysis.

Another type of wave that might be present is the dispersive Alfvén wave at frequencies much below the ion oxygen frequencies. Using a method similar to ours but comparing theory only with the ratio of the wave electric and magnetic fields, the Doppler shift of these waves has been shown to be consistent with some broadband emissions (Stasiewicz et al., 2000; Lund et al., 2001; Stasiewicz and Khotyaintsev, 2001). It is not clear that this model, even in principle, can explain waves with dominating E$_{||}$, but dispersive Alfvén waves and other low frequency modes should be included in future, more complete studies of broadband waves.

10   Conclusions

We use Cluster observations to study broadband waves at an altitude of about 4 R_E in the nightside auroral region. A detailed study of frequencies between 10 Hz (slightly above the proton gyrofrequency) and 180 Hz (approximately the lower hybrid frequency) during a 40-min long event gives several interesting conclusions.

Much of the broadband wave activity has a larger electric field perpendicular ($\delta E_\perp$) than parallel ($\delta E_{||}$) to the geomagnetic field, consistent with several earlier studies. However, we find that $\delta E_{||}$ dominates in some regions. The waves with mainly a parallel electric field and a parallel **k**-vector are consistent with ion acoustic and oblique ion acoustic waves. Waves at larger angles to the parallel direction are well described as Electrostatic Ion Cyclotron (EIC) waves (see also a preliminary study by Backrud et al., 2004). Furthermore, observed electron beams can generate all the observed waves.

The ion acoustic and oblique ion acoustic waves are observed only in regions without suprathermal (tens of eV) electrons. This agrees with textbook plasma physics, stating that even small amounts of suprathermal and cold plasma will damp ion acoustic waves. Our combined wave and particle observations explain why such waves can occur in parts of the auroral region.

The regions void of suprathermal plasma are interpreted as magnetic flux tubes where the electrons above the spacecraft are accelerated downward and the suprathermal ionospheric electrons below the spacecraft cannot penetrate a barrier at the bottom of a potential drop of a few hundred volts in total. In our wave study the lack of suprathermal electrons is important for the generation of ion acoustic waves. We also note that clear signatures of auroral acceleration regions at this high altitude have not been reported before.

As opposed to ion acoustic waves, EIC waves occur in regions with a mixture of hot (keV) and suprathermal electron populations. Thus, our study shows a clear correlation between a mixture of hot and suprathermal electrons and EIC waves, and also between the presence of only hot electrons and ion acoustic waves. Future statistical studies might use this observation, and obtain rather detailed properties of broadband waves from electron observations, or vice versa.

Summarizing our observational and theoretical findings we conclude that many of the broadband emissions are well described as a mixture of essentially electrostatic modes which all correspond to different parts of the same dispersion surface in the linear theory of waves in a homogeneous plasma. In particular, ion acoustic waves occur in regions without suprathermal electrons and EIC waves in regions with a mixture of suprathermal and hot electrons.

References

André. M. and Yau, A.: Theories and observations of ion energisation and outflow in the high latitude magnetosphere, Space Sci. Rev., 80, 27–48, 1997.

André. M.: Dispersion surfaces, Plasma Phys., 33, 1–19, 1985.

Backrud, M., Tjulin, A., Vaivads, A., et al.: Interferometric Identification of Ion Acoustic Broadband Waves in the Auroral Region:

CLUSTER Observations, Geophys. Res. Lett., 32(21), L21109, doi:10.1029/2005GL022640, 2005.

Backrud, M., André, M., and Balogh, A., et al.: Identification of broadband waves above the auroral acceleration region: Cluster observations, Ann. Geophys., 22, 4203–4216, 2004, **SRef-ID: 1432-0576/ag/2004-22-4203**.

Balogh, A., Dunlop, M. W., Cowley, S. W. H., et al.: The Cluster Magnetic Field Investigation., Space Sci. Rev., 79, 65-91, 1997.

Bergmann, R., Roth I., and Hudson, M. K.: Linear stability of the H(+)–O(+) two-stream interaction in a magnetized plasma, J. Geophys. Res., 93, 4005–4020, 1988.

Bonnell, J., Kintner, P. M., Wahlund, J.-E., et al.: Interferometric determination of broadband ELF wave phase velocity within a region of transverse auroral ion acceleration, Geophys. Res. Lett., 23, 3297–3300, 1996.

Brambilla, M.: Kinetic theory of plasma waves, Oxford Science Publications, 1998.

Cornilleau-Wehrlin, N., Chauveau, P., Louis, S., et al.: The Cluster Spatial-Temporal Analysis on Field Fluctuations Experiment., Space Sci. Rev., 79, 107–136, 1997.

Décréau, P. M. E., Fergeau, P., Krannosels'kikh, V., et al.: WHISPER, a resonance sounder and wave analyzer: Performance and perspectives for the Cluster mission, Space Sci. Rev., 79, 157–193, 1997.

Escoubet, C. P., Schmidt, R., and Goldstein, M. L.: Cluster- Science and mission overview, Space Sci. Rev., 79, 11–32, 1997.

Ganguli, G., Slinker, S., Gavrishchaka, V., et al.: Low frequency oscillations in plasma with spatially variable field-aligned flow, Physics of Plasmas, 9, 2321–2329, 2002.

Gray, P. C., Hudson, M. K., Bergmann, R., et al.: Simulation study of ion 2-stream instability in the auroral acceleration region, , Geophys. Res. Lett., 17, 1609–1612, 1990.

Gurnett, D. A. and Frank, L. A.: A region of intense plasma wave turbulence on auroral field lines, J. Geophys. Res., 82, 1031, 1977.

Gustafsson, G., Boström, R., Holback, B., et al.: The electric field and wave experiment for the Cluster mission, Space Sci. Rev., 79, 137–156, 1997.

Janhunen, P., Olsson, A., and Laakso, H.: The occurrence frequency of auroral potential structures and electric fields as a function of altitude using Polar/EFI data, Ann. Geophys., 22, 1233–1250, 2004, **SRef-ID: 1432-0576/ag/2004-22-1233**.

Janhunen, P., Olsson, A., Mozer, F. S., and Laakso, H.: How does the U-shaped potential close above the acceleration region? A study using Polar data, Ann. Geophys., 17, 1276–1293, 1999, **SRef-ID: 1432-0576/ag/1999-17-1276**.

Johnstone, C., Alsop, S., Burge, P. J., et al.: The electric field and wave experiment for the Cluster mission, Space Sci. Rev., 79, 351–398, 1997.

Kindel, J. M. and Kennel, C. F.: Topside current instabilities, J. Geophys. Res., 76, 3055–3078, 1971.

Kintner, P. M., Franz, J., Schuck, P., and Klatt, E.: Interferometric coherency determination of wavelength or what are broadband ELF waves?, J. Geophys. Res., 105, 21 237–21 250, 2000.

Kintner, P. M., Bonnell, J., Arnoldy, R., et al.: SCIFER-Transverse ion acceleration and plasma waves, Geophys. Res. Lett., 23, 1873–1876, 1996.

Knudsen, D. J., Clemmons, J. H., and Wahlund, J.-E.: Correlation between core ion energization, suprathermal electron bursts, and broadband ELF plasma waves, J. Geophys. Res., 103, 4171–4186, 1998.

Lund, E. T.: Comment on "Identification of widespread turbulence of dispersive Alfvén waves" by Stasiewicz, K., et al., Geophys. Res. Lett., 28, 1403–1404, 2001.

Marklund, G. T., Karlsson, T., Figueiredo, S., Johansson, T., et al.: Characteristics of quasi-static potential structures observed in the auroral return current region by cluster, Nonlin. Processes Geophys., 11, 709–720, 2004, **SRef-ID: 1607-7946/npg/2004-11-709**.

Oscarsson, T. and K. Rönnmark: Reconstruction of Wave Distribution Functions in Warm Plasmas, J. Geophys. Res., 94, 2417–2427, 1989.

Oscarsson, T.: Dual Principles in Maximum Entropy Reconstruction of the Wave Distribution Function, J. Comput. Phys., 110, 221–233, 1994.

Reme, H., Bosqued, J. M., Sauvaud, J. A.: The Cluster Ion Spectrometry (CIS) experiment, Space Sci. Rev., 79, 303–350, 1997.

Rönnmark, K.: WHAMP- Waves in Homogeneous Anisotropic, Multicomponent Plasmas, KGI Report 179, Kiruna Geophysical Institute, 1982.

Stenberg, G, Oscarsson, T., André, M., and Chaston, C. C.: Investigating wave data from the FAST satellite by reconstructing the wave distribution function, J. Geophys. Res., 107(A8), 1190, doi:10.1029/2001JA900154, 2002.

Stasiewicz, K., Khotyaintsev, Y., Berthomier, M., and Wahlund, J.-E.: Identification of Widespread Turbulence of Dispersive Alfvén Waves, Geophys. Res. Lett., 27, 173–176, 2000.

Stasiewicz K. and Khotyaintsev, Y.: Reply to comment on "Identification of widespread turbulence of dispersive Alfvén waves", Geophys. Res. Lett., 28, I7, 1405–1406, 2001.

Wahlund, J.-E., Yilamaz, A., Backrud, M., et al.: Observations of auroral broadband emissions by CLUSTER, Geophys. Res. Lett., 30, 1563–1566, 2003.

Wahlund, J.-E., Eriksson, A. I., Holback, B., et al.: Broadband ELF plasma emission during auroral energization 1. Slow ion acoustic waves, J. Geophys. Res., 103, 4343–4375, 1998.